

X-ray constraints on the spectral energy distribution of the $z = 5.18$ blazar SDSS J013127.34–032100.1

HONGJUN AN¹ AND ROGER W. ROMANI²

¹*Department of Astronomy and Space Science, Chungbuk National University, Cheongju, 28644, Republic of Korea*

²*Department of Physics/KIPAC, Stanford University, Stanford, CA 94305-4060, USA*

ABSTRACT

We report on X-ray measurements constraining the spectral energy distribution (SED) of the high-redshift $z = 5.18$ blazar SDSS J013127.34–032100.1 with new *XMM-Newton* and *NuSTAR* exposures. The blazar’s X-ray spectrum is well fit by a power law with $\Gamma = 1.9$ and $N_{\text{H}} = 1.1 \times 10^{21} \text{ cm}^{-2}$, or a broken power law with $\Gamma_l = 0.5$, $\Gamma_h = 1.8$, and a break energy $E_b = 0.7 \text{ keV}$ for an expected absorbing column density of $N_{\text{H}} = 3.6 \times 10^{20} \text{ cm}^{-2}$, supported by spectral fitting of a nearby bright source. No additional spectral break is found at higher X-ray energies (1–30 keV). We supplement the X-ray data with lower-energy radio-to-optical measurements and *Fermi*-LAT gamma-ray upper limits, construct broadband SEDs of the source, and model the SEDs using a synchro-Compton scenario. This modeling constrains the bulk Doppler factor of the jets to ≥ 7 and ≥ 6 (90%) for the low- and high- N_{H} SEDs, respectively. The corresponding beaming implies ≥ 130 (low N_{H}) or ≥ 100 (high N_{H}) high-spin supermassive black holes similar to J0131 exist at similar redshifts.

Keywords: Active galactic nuclei (16), High energy astrophysics (739), Blazars (164), Spectral energy distribution (2129)

1. INTRODUCTION

Supermassive black holes exist even at high redshifts (e.g., $z \geq 5$; Fan et al. 2001). Rapidly spinning black holes may power bipolar jets via the Blandford-Znajek mechanism (Blandford & Znajek 1977); when these jets lie close to the Earth line of sight (LoS) these are visible as bright ‘blazars’ (Urry & Padovani 1995). These jets are relativistic, accelerating high energy particles which interact with magnetic field and ambient photons, and producing broadband emission which is further enhanced by Doppler beaming due to relativistic bulk motion. This emission can be bright across the electromagnetic spectrum, allowing detection to very high redshifts (e.g., $z = 5.48$; Romani et al. 2004).

Blazars’ broadband spectral energy distributions (SEDs) exhibit a characteristic double-hump spectrum, one at low frequencies (<X-rays) and another at higher frequencies. The former is believed to be produced by synchrotron radiation of the accelerated particles, and the latter by inverse-Compton upscattering of soft photons from the synchrotron radiation

(synchrotron self-Compton; SSC), and the torus, disk, and broad line region (external Compton; EC) by the jet particles (e.g., Boettcher et al. 1997). This scenario has been used to model SEDs of high- z blazars (Romani 2006; Sbarrato et al. 2013; Ghisellini et al. 2015; An & Romani 2018). The emission is relativistically beamed due to the bulk motion of the jet by the Doppler factor $\delta = 1/[\Gamma_D(1 - \sqrt{1 - 1/\Gamma_D^2} \cos\theta_V)]$, where Γ_D is the jet Lorentz factor, and θ_V is the viewing angle; these parameters are crucial for estimating the jet luminosity and beaming factor, and are determined from the SED peak frequencies and amplitudes via SED modeling. The shape of the SED is determined by conditions in the emission zone, is sensitive to variations in these conditions, and is modified by the environment (e.g., soft photon fields) along the LoS. Therefore the SEDs probe the source emission zone properties as well as the extragalactic background via emission (e.g., Ghisellini et al. 2015), variability (e.g., Liodakis et al. 2018) and absorption (e.g., Fermi-LAT Collaboration et al. 2018) studies.

High-redshift (high- z) blazars with well-measured SEDs are very useful in understanding the early universe and its evolution. In particular, SED studies of high- z blazars provide estimates of their jet δ ’s (e.g., Romani 2006; Ghisellini et al. 2015; An & Romani 2018). For these high-power sources the characteristic double-hump

Corresponding author: Hongjun An
hjan@cbnu.ac.kr

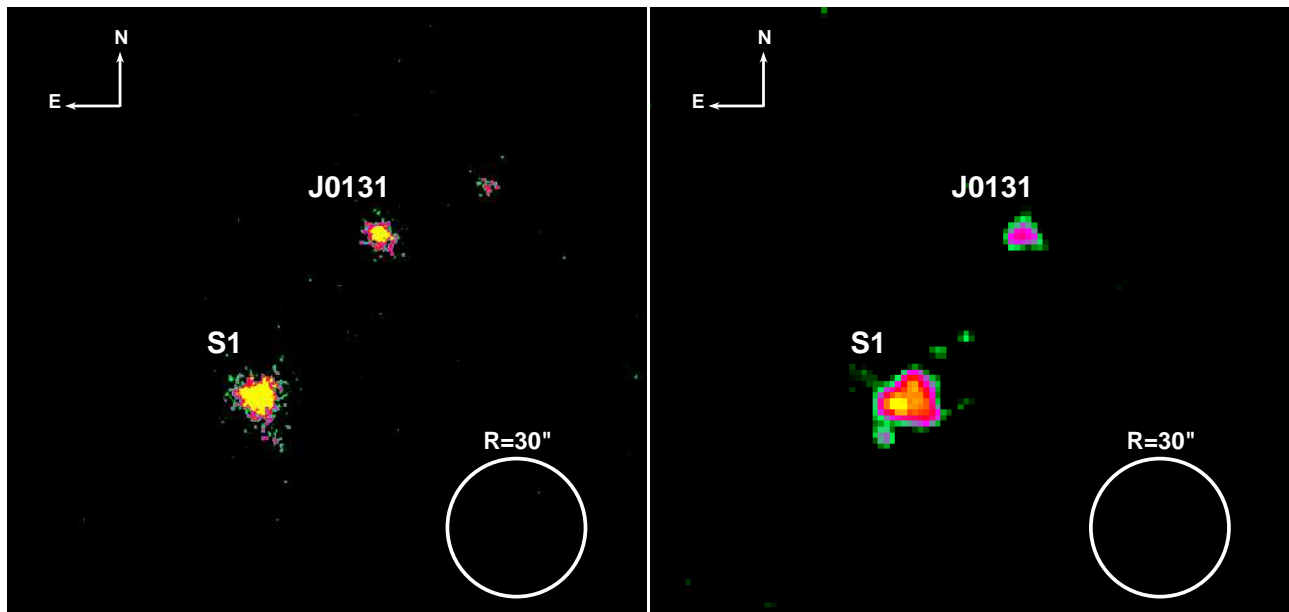


Figure 1. 0.2–10 keV and 3–30 keV images taken with *XMM*/MOS (left) and *NuSTAR* (right). J0131 is detected up to ~ 30 keV, and another brighter source (S1) is visible at $\sim 90''$ south east of J0131. The images are smoothed and scales are adjusted for better legibility. An $R = 30''$ white circle is drawn in the lower right corner for reference. Note that the south source “S1” appears to have an extended emission (south-west jet-like structure) in the *XMM* image. Our investigations with the *XMM*/OM images suggest that the structure may be produced by contamination from another faint point source near the tip of the structure.

spectrum has a synchrotron peak in the far-IR to optical band and a high-energy Compton peak in the X-ray to γ -ray band. The X-rays are thought to probe the SSC SED and possibly the rising tail of the EC emission, and the peak locations of the high-energy humps with respect to the low-energy synchrotron one are sensitively dependent on Γ_D . Thus, good coverage of these peaks is required for Γ_D measurements. Since the black hole masses can be estimated from SED and spectroscopic studies and since a strong jet is generally assumed to be related to high spin, the population of luminous high- z blazars tells us much about the origin and growth mechanisms (e.g., Berti & Volonteri 2008) of high mass, high spin holes in the early universe. While such blazars are rare (only four at $z > 5$ have been reported to date), with a beaming correction $\approx 2\Gamma_D^2$, they represent a substantial population.

SDSS J013127.34–032100.1 (J0131 hereafter) is an optically luminous high- z blazar ($z = 5.18$; Yi et al. 2014). Its broadband SED exhibits the characteristic double-hump structure with strong disk emission in the optical band. Previous SED modelings, using existing *Neil-Gehrels-Swift* X-ray observatory (XRT; Burrows et al. 2005) data, have been used to infer a modest jet Doppler factor ($\delta \geq 10$; Ghisellini et al. 2015). These X-ray data only poorly constrained the Compton component, so Doppler factor constraints were quite weak. We therefore observed the source with *XMM-Newton* (Jansen et al. 2001) and *NuSTAR*

(Harrison et al. 2013) to improve the X-ray SED characterization. We then combine multi-waveband data, construct broadband SEDs, and model with a synchro-Compton code (Boettcher et al. 1997) to better constrain the jet Doppler factor.

We describe the data reduction and analyses in §2. The broadband SEDs are constructed and modeled in §3. We conclude by discussing the population implications in §4.

2. DATA REDUCTION AND ANALYSIS

2.1. X-ray data reduction

We obtained contemporaneous 50 ks *XMM* and 100 ks *NuSTAR* exposures on MJD 58847.3. The *XMM* data are processed with the `emproc` and `eproc` tools of SAS 20190531_1155, and particle flares are removed following the standard procedure.¹ The exposures after this process are 43 ks, 43 ks and 32 ks for the MOS1, MOS2 and PN data, respectively. We process the *NuSTAR* data using the `nupipeline` tool in HEASOFT 6.26.1, setting `saamode=strict` and `tentacle=yes` as recommended by the *NuSTAR* SOC.² This reduces the exposure to 80 ks. J0131 is faint but

¹ <https://www.cosmos.esa.int/web/xmm-newton/sas-thread-epic-filterbackground>

² http://www.srl.caltech.edu/NuSTAR_Public/NuSTAROperationSite/SAA_Filtering/SAA_Filter.php

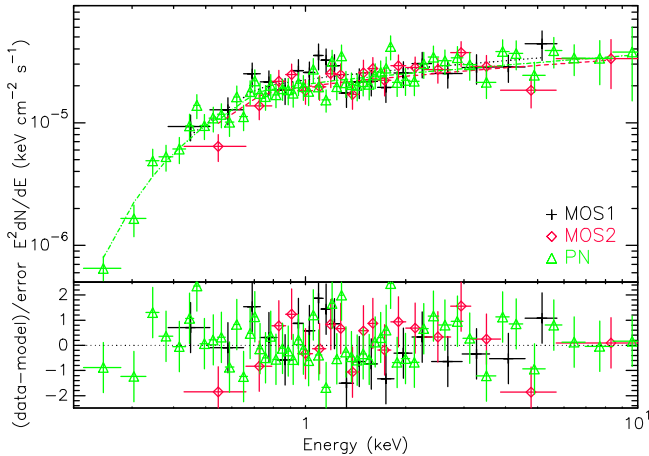


Figure 2. 0.2–10 keV SED measured with *XMM* MOS1 (black), MOS2 (red), and PN (green). *Top*: SED data (data points) and the best-fit BPL model (lines). *Bottom*: fit residuals.

clearly visible in the cleaned images, and a brighter second source is detected $\sim 90''$ south east of J0131 (Fig. 1). We note that the south Atlantic anomaly (SAA) filter setting for the *NuSTAR* process does not have large impact on our results below.

2.2. Spectral analysis for the *XMM* data

We first measure 0.2–10 keV spectra of J0131 using the *XMM* data. We extract events within $R = 16''$ and $R = 32''$ radius circles for the source and background, respectively, and compute the corresponding response files with the `arfgen` and `rmfgen` tasks of SAS. The source spectra are grouped to have at least 20 counts per bin, and we fit the spectra with an absorbed power-law (PL) model using `wilm` abundance (Wilms et al. 2000) and `vern` cross section (Verner et al. 1996) in XSPEC 12.10.1. Because *XMM* provides high-quality data at low energies (< 1 keV), we allow the absorbing column density N_{H} to vary and then cross-check the inferred value with Galactic HI and optical extinction measurements.

We find that the model fits the data well ($\chi^2/\text{dof}=69/90$) with $N_{\text{H}} = (1.1 \pm 0.2) \times 10^{21} \text{ cm}^{-2}$, $\Gamma = 1.89 \pm 0.07$ and unabsorbed flux $F_{3-10 \text{ keV}} = (6.1 \pm 0.6) \times 10^{-14} \text{ erg cm}^{-2} \text{ s}^{-1}$ (Table 1). We also try to fit the spectra with a broken power-law (BPL) model, but the model does not improve the PL fit at all (Table 1), meaning that a simple PL is adequate. While this model is quite acceptable, we find that the fit N_{H} value is significantly larger than the $\sim 3.5 \times 10^{20} \text{ cm}^{-2}$ expected in this area from radio HI mapping.³ The finer scale of the PannSTARS2 dust maps (Green et al. 2019) shows patchy extinction in this direction, with low ab-

sorption at the blazar position, but values as large as $N_{\text{H}} = 10^{21} \text{ cm}^{-2}$ within $30'$.

A check on the N_{H} in this direction is provided by a nearby bright(er) source $\sim 90''$ south east of J0131 (“S1” in Fig. 1). We extract the source and background spectra with $R = 16''$ and $R = 32''$ radius circles, and generate the corresponding response files using the procedure described above. The observed X-ray spectra of this source appear to be a PL or a BPL, so we fit the spectra with both models. The PL fit gives $N_{\text{H}} = (2.3 \pm 0.4) \times 10^{20} \text{ cm}^{-2}$, $\Gamma = 1.80 \pm 0.03$, and $F_{3-10 \text{ keV}} = (1.36 \pm 0.07) \times 10^{-13} \text{ erg cm}^{-2} \text{ s}^{-1}$ ($\chi^2/\text{dof}=182/220$), while the BPL model has $N_{\text{H}} = (3.6 \pm 0.6) \times 10^{20} \text{ cm}^{-2}$, $\Gamma_l = 1.98 \pm 0.07$, $\Gamma_h = 1.59 \pm 0.08$, $E_b = 1.9 \pm 0.4 \text{ keV}$, and $F_{3-10 \text{ keV}} = (1.5 \pm 0.1) \times 10^{-13} \text{ erg cm}^{-2} \text{ s}^{-1}$ ($\chi^2/\text{dof}=168/218$). The BPL provides a significantly better fit (f -test probability of 2×10^{-4}). Note that the N_{H} values inferred from these models (toward S1) are significantly lower than that inferred for J0131, and the BPL S1 model N_{H} agrees very well with the Galactic HI estimate. Adding *NuSTAR* data in the fits does not alter the results for S1.

We therefore have fit the *XMM* J0131 spectra with N_{H} fixed at $3.6 \times 10^{20} \text{ cm}^{-2}$. A PL model with $\Gamma = 1.63 \pm 0.04$ has $\chi^2/\text{dof}=98/91$ but residual trends at low and high energies are clearly visible. Accordingly, we then apply a BPL model and find that a model with $\Gamma_l = 0.5 \pm 0.4$, $\Gamma_h = 1.78 \pm 0.05$, $E_b = 0.7 \pm 0.1 \text{ keV}$, and $F_{3-10 \text{ keV}} = (6.7 \pm 0.6) \times 10^{-14} \text{ erg cm}^{-2} \text{ s}^{-1}$ (Table 1 and Fig. 2) provides a significantly better fit (f -test probability of 2×10^{-7}). In summary, PL with large $N_{\text{H}} = (1.1 \pm 0.2) \times 10^{21} \text{ cm}^{-2}$ or BPL with small $N_{\text{H}} = (3.6 \pm 0.6) \times 10^{20} \text{ cm}^{-2}$ can fit the *XMM* spectra of J0131 well.

2.3. Analysis of the *NuSTAR* data

We next analyze the *NuSTAR* data. The *NuSTAR* spectra of J0131 are obtained with an $R=15''$ region. We use a small aperture in order to minimize contamination from S1. Background spectra are obtained using an $R = 45''$ aperture in a source-free region on the same detector chip. The corresponding response files are generated with the `nuproduct` tool. We group the *NuSTAR* spectra to have at least 5 counts per bin and fit the spectra with a single PL model employing l statistic (Loredo 1992) in XSPEC. The model describes the data well with $\Gamma = 1.67 \pm 0.28$ and $F_{3-10 \text{ keV}} = (7.1 \pm 1.4) \times 10^{-14} \text{ erg cm}^{-2} \text{ s}^{-1}$ (Table 1).

The *NuSTAR* spectral analysis results for J0131 may sensitively depend on the extraction regions for the faint source and non-uniform background (Fig. 1), so we applied various source and background regions as a sanity

³ <https://heasarc.gsfc.nasa.gov/cgi-bin/Tools/w3nh/w3nh.pl>

Table 1. Summary of X-ray spectral fits

Data ^a	model	Energy (keV)	N_{H} (10^{22}cm^{-2})	Γ_l	E_b (keV)	Γ_h	$F_{3-10\text{ keV}}$ ($10^{-14}\text{ erg cm}^{-2}\text{ s}^{-1}$)	χ^2/dof	Comments
X	PL	0.2–10	0.11 ± 0.02	1.89 ± 0.07	6.1 ± 0.6	69/90	large N_{H}
X	BPL	0.2–10	0.17 ± 0.05	2.3 ± 0.4	1.4 ± 0.4	1.8 ± 0.1	6.6 ± 0.7	67/88	large N_{H}
X	PL	0.2–10	0.036^{b}	1.63 ± 0.04	8.0 ± 0.6	98/91	small N_{H}
X	BPL	0.2–10	0.036^{b}	0.5 ± 0.4	0.7 ± 0.1	1.78 ± 0.05	6.7 ± 0.6	70/89	small N_{H}
N	PL	3–30	0.11^{b}	1.7 ± 0.3	7.1 ± 1.4	23/27	insensitive to N_{H}
X,S,N	PL	0.2–30	0.11 ± 0.02	1.86 ± 0.07	6.1 ± 0.6	337/382	large N_{H}
X,S,N	BPL	0.2–30	0.036^{b}	0.7 ± 0.3	0.7 ± 0.1	1.78 ± 0.05	6.4 ± 0.6	337/381	small N_{H}

^a X: *XMM*, N: *NuSTAR*, S: *Swift*

^b Frozen

check. We shift the source region by 1 pixel ($\approx 2.5''$) in each direction to generate nine new regions and select nine background regions with varying size and location on the same detector chip. We then perform spectral analyses for the 81 combinations of the source and background regions, and find an average $\Gamma = 1.64$ and the standard deviation 0.14. The former is similar to the best-fit value and the latter is significantly smaller than the fit uncertainty (Table 1). We therefore conclude that the *NuSTAR* fit results in Table 1 represent the source spectra well.

The source is not detected by *NuSTAR* above ~ 30 keV, so we derive a flux upper limit in the 30–79 keV band. Holding all spectral parameters fixed at the low-energy best-fit values (Table 1) except for the flux, we use the `steppar` command in `XSPEC` to find the 90% flux upper limit $F_{30-79\text{ keV}} = 4.8 \times 10^{-13}\text{ erg cm}^{-2}\text{ s}^{-1}$. This value is insensitive to the assumed spectral index.

2.4. Joint fits of the broadband data

To further constrain the broadband X-ray spectrum, we jointly fit all X-ray data including archival *Swift* exposures (taken from An & Romani 2018, AR18 hereafter). Note that we allow a `const` in the model to account for cross normalization among the instruments; these cross-calibration constants are statistically consistent with 1 in the fits summarized below. For the large N_{H} case, the combined data are well fit with a simple PL model having spectral parameters consistent with the *XMM*-estimated values; a spectral break (i.e., BPL fit) is unnecessary (f -test $p=0.4$). For the small N_{H} case the fit is dominated by the high-count *XMM* data, with fit parameters consistent with those of a simple *XMM*. The results are summarized in Table 1, and the X-ray SEDs are presented in Figure 3: BPL with small N_{H} (top) and simple PL with large N_{H} (bottom).

3. BROADBAND SED CHARACTERIZATION

We supplement the X-ray data with archival radio-optical and *Fermi*-LAT data (§ 3.1). The two SEDs

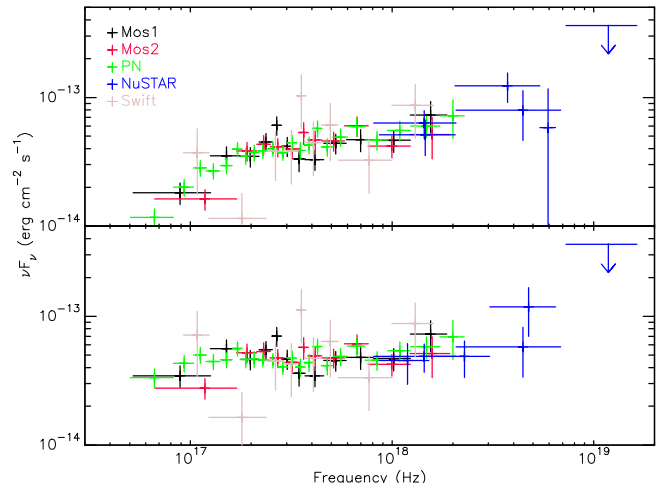


Figure 3. 0.2–30 keV SEDs for the low- N_{H} BPL (top) and high- N_{H} PL (bottom) models.

differ only in the X-ray band. The low- N_{H} SED exhibits a rapidly rising trend at low X-ray energies, while the high- N_{H} one shows a broad flat X-ray component (Fig. 3). Our new SED measurements provide better coverage of the X-rays. However, the low-frequency ($< 5 \times 10^{13}$ Hz) and the gamma-ray SED are not well measured, limiting the accuracy of our inferred jet properties.

We assume that the broadband emission (Fig. 4) is produced by synchrotron and Compton emission by the jet electrons with an addition of disk emission in the optical band at $\sim 10^{14}$ Hz (§ 3.2). The low-frequency $< 10^{13}$ Hz emission is attributed to synchrotron radiation, and the X-rays ($10^{16} - 10^{19}$ Hz) and undetected gamma rays ($> 10^{19}$ Hz) are assumed to be produced by the SSC and disk EC processes, respectively (§ 3.3 and 3.4). Alternatively, the X-ray emission may be attributed to the disk-EC process (e.g., Ghisellini et al. 2015), and we consider this possibility as well (§ 3.5).

3.1. Construction of the broadband SEDs of J0131

The radio-to-optical measurements and *Fermi*-LAT upper limits are taken from previous works (AR18; Zhang et al. 2017). Thus, the principal SED updates are the revised X-ray measurements. Note that the X-ray spectra are produced by `eeufspec` command in `XSPEC` and corrected for the absorption. The resulting SEDs are shown in Figure 4.

The SED shape can provide important constraints on the jet properties such as the magnetic-field strength B and δ . In particular, the peak frequencies of the SED humps are very useful for inferring δ . Without good SED coverage, the peak frequencies alone do not allow precise determination of δ , but we can still use the frequency scaling presented in AR18 to roughly estimate the electron Lorentz factor (γ_e) and bulk Doppler factor: $\gamma_e \approx (\nu_{ssc,pk}^{obs}/\nu_{sy,pk}^{obs})^{1/2}$ and $\delta \approx (\nu_{EC,pk}^{obs}/\nu_{BB,pk}^{obs})^{1/2}/\gamma_e$, where $\nu_{X,pk}^{obs}$ is the “observed” peak frequency of the emission component ($X = ssc$ for synchro-self-Compton, $X = sy$ for synchrotron, $X = EC$ for external Compton, and $X = BB$ for disk emission). However, unlike QSO J0906+6930 studied by AR18, the synchrotron SED of J0131 is poorly measured and $\nu_{sy,pk}^{obs}$ not well constrained. To make progress we assume that $\nu_{sy,pk}^{obs} < 10^{14}$ Hz similar to other high- z blazars, $\nu_{ssc,pk}^{obs} \approx 10^{18}$ Hz, $\nu_{BB,pk}^{obs} \approx 3 \times 10^{14}$ Hz, and $\nu_{EC,pk}^{obs} \approx 10^{20-22}$ Hz as an initial guess. We can then infer that $\gamma_e \geq 100$ and $\delta \leq 30$. These rough estimates, obtained based only on the observed peak frequencies, serve as a guide for SED model computation and are superseded by the more detailed modeling below.

3.2. The SED model

The model computation is performed with a blazar SED code adapted from Boettcher et al. (1997). Electrons and positrons (e^\pm) with a power-law energy distribution $dN_e/d\gamma_e \propto \gamma_e^{-p_1}$ are injected at an assumed height of $h = 0.03$ pc from the black hole and cooled by radiation while they travel along the jet. Hence, the energy distribution of the particles changes with time, and we follow the particle distribution and compute the emission for 10^7 sec. In addition to the jet emission, the model computes the disk emission in the 10^{14-15} Hz optical band assuming a standard Shakura-Sunyaev disk (Shakura & Sunyaev 1973) for $M_\bullet = 1.5 \times 10^{10} M_\odot$ (e.g., Ghisellini et al. 2015; Campitiello et al. 2018), where the disk luminosity is adjusted to match the optical SED; the disk emission is held fixed when modeling the jet emission below. The time-integrated model SED is then compared to the observations, and we adjust the model parameters to attain a match. Note again that the X-ray SED is attributed to the SSC (§ 3.3 and 3.4) or EC (§ 3.5) process.

Because of the lack of SED measurements in some wavebands and covariance among the model parameters, they are not all well constrained; we thus also make the common assumptions of magnetic equipartition and $\Gamma_D = \delta$. We further assume that the e^\pm spectral index p_1 should be ≥ 1 since acceleration theory does not produce very hard energy distribution for the injected particles.

We start with previously-estimated parameters for J0131 (AR18) and the assumptions above, and vary the e^\pm Lorentz factors γ_e 's, spectral index for the distribution p_1 , particle number density n_e , the emitting volume R_b , and δ to match the observed SED. Because the parameter space is large and the parameters co-vary, simultaneously optimizing all parameters is unfeasible. We therefore specify a δ , Monte Carlo (MC) vary the other parameters, calculate the model χ^2 in the IR (a *WISE*/W3 measurement at $\sim 2.5 \times 10^{13}$ Hz) and X-ray bands. In a downward descent, the next trial parameters are generated, by varying around values for the minimum χ^2 model to that point. This procedure gives minimum χ^2 model parameters for each δ . Note that the optical points are disk-dominated and so are not used in this jet fit, except that the model must not exceed these optical fluxes. We scan δ over the range 4–60 which is wide enough to cover the previous estimate of $\delta \approx 4$ –16 (AR18) and the rough estimate presented above (§ 3.1).

Because the disk emission is strong compared to the synchrotron, the EC flux is large and often violates the LAT upper limits unless B is also large so that the e^\pm are efficient synchrotron/SSC radiators. Note that synchro-Compton cooling is efficient (large B and L_{disk}), so the synchrotron and SSC SEDs become fairly narrow. Examples of optimized models for specific δ are displayed in Figure 4, and the model parameters are presented in Table 2.

3.3. The low- N_H SED model

As noted above, we optimize the SED models by scanning δ values and minimizing χ^2 over the other parameters. We find a global minimum $\chi_{\text{min}}^2 = 68$ (60 dofs) at $\delta = 27$ (top panels of Fig. 4). The model χ^2 converges better with low δ 's than with high ones (≥ 20); the high- δ models often fall into a local minimum. The general trend for the parameters is that n_e (and B) increases while the other parameters decrease with increasing δ . The parameters for a few δ values are presented in Table 2.

The behavior of the SED models for different δ values is complex but can be qualitatively explained as follows. In the low- δ models, EC emission is relatively weak and the X-ray SED is easily matched by the SSC. So the χ^2

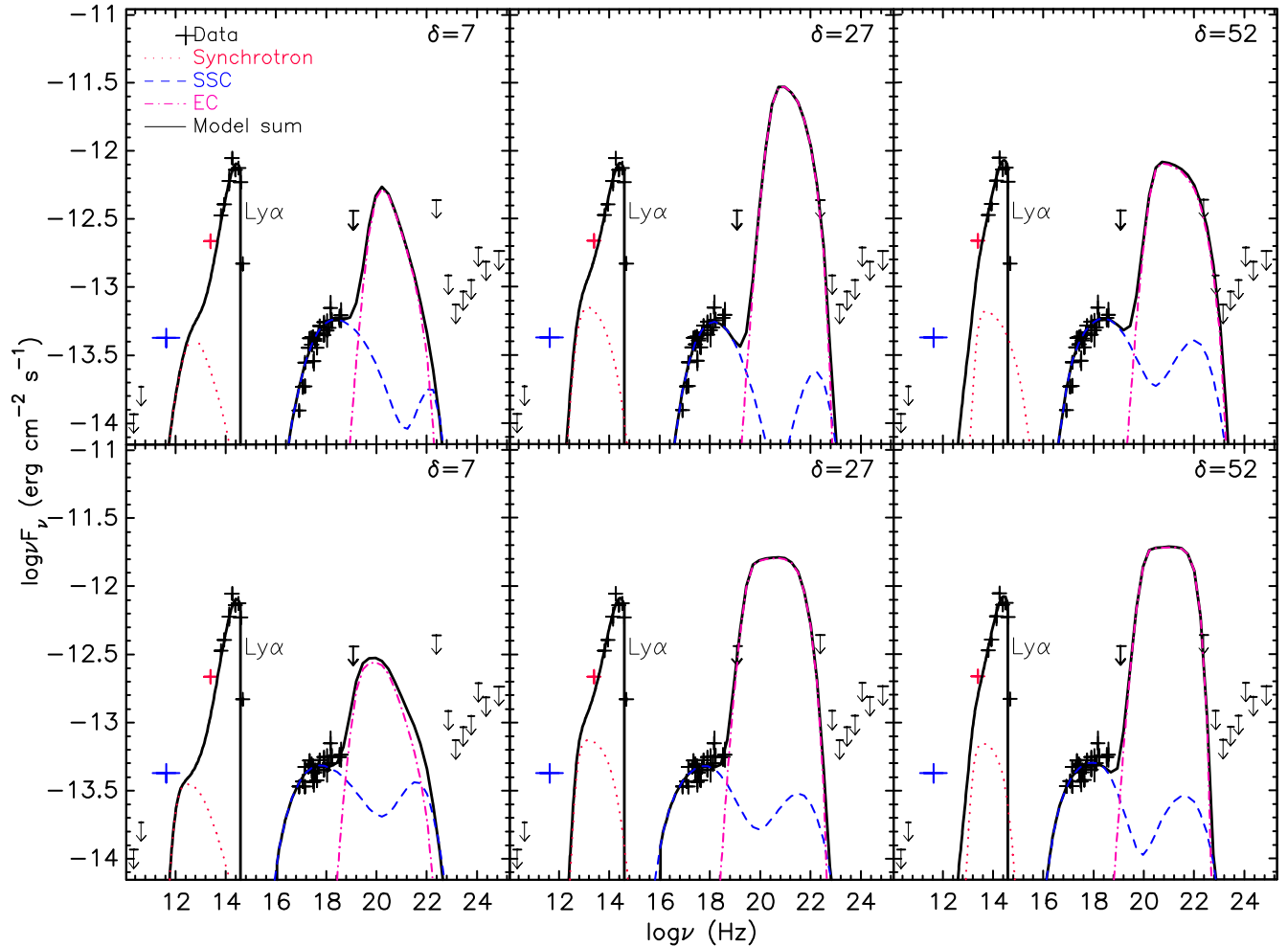


Figure 4. Examples of broadband SED data and models ($\delta=7, 27,$ and 52 from left) for J0131. The X-ray data are rebinned for better legibility and the *WISE*/W3 point is plotted in red. *Top*: Low- N_{H} SED and models. *Bottom*: High- N_{H} SED and models. 95% upper limits are plotted as down arrows. The SED models are displayed in black solid lines, and the model components are also presented: synchrotron (red dotted), SSC (blue dashed), and EC (pink dot-dashed) emission. The blue point is a *PLANCK* flux near the source, which can be taken as an upper limit.

is determined primarily by the *WISE*/W3 data point. Changing the model parameters (e.g., B) from the optimal values degrades the fit. Lowering B requires larger γ_e 's (i.e., a shift of $dN_e/d\gamma_e$ in the high- γ_e direction) to preserve the X-ray data match (i.e., $\nu_{\text{ssc},pk}$), but $\nu_{\text{sy},pk}$ lowers because $\nu_{\text{ssc},pk}/\nu_{\text{sy},pk} \propto \gamma_e^2$, which worsens the match to the *WISE* point. On the other hand, increasing B does the opposite, making the γ_e 's smaller and $\nu_{\text{sy},pk}$ larger; so a better match to the *WISE* point is expected. However, n_e also increases to preserve equipartition, which then lowers the synchrotron flux F_{sy} for the given SSC flux F_{ssc} (X-ray data) because $F_{\text{ssc}}/F_{\text{sy}} \propto n_e$. With EC this last relationship is not exact, but is adequate for the weak EC emission seen in low- δ high- B models. This allows a reliable determination of a 90% lower limit $\delta > 7$ ($\Delta\chi^2 = 11$ for 6 dofs).

As δ increases, the separation between the SSC and EC peaks grows. With the SSC component set by the X-ray measurements, EC emission encroaches on the LAT band in high- δ models (Fig. 4). As noted above, lowering B increases γ_e 's, pushing the EC emission to higher flux and frequencies which degrades the fit. Increasing B typically improves the fit by lowering the EC flux and frequency. Although the *WISE* point remains a concern in high- B models, unlike the low- δ case these models can accommodate it because we no longer have $F_{\text{ssc}}/F_{\text{sy}} \propto n_e$ (EC emission dominates). Thus we find an acceptable fit even for the highest $\delta=60$ investigated.

However, continued B (and δ) increase will create model problems; (1) $\nu_{\text{sy},pk}$ becomes too high to accommodate the *WISE* point, (2) when the EC emission is sufficiently suppressed, $F_{\text{ssc}}/F_{\text{sy}} \propto n_e$, and we must lower the synchrotron emission to keep the X-ray

Table 2. Parameters for the SED models in Figure 4

Parameter	Symbol	Value					
Redshift	z	5.18					
Black Hole mass (M_{\odot})	M_{\bullet}	1.5×10^{10}					
Disk Luminosity (erg/s)	L_{disk}	1.1×10^{48}					
SED model		low N_{H}			high N_{H}		
Doppler factor	δ	7	27	52	7	27	52
Magnetic field (G)	B	15	30	110	19	41	72
Comoving radius of blob (cm)	R'_b	7.1×10^{14}	1.3×10^{14}	2.2×10^{13}	6.6×10^{14}	1.3×10^{14}	5.9×10^{13}
Effective radius of blob (cm)	R'_E ^a	4.8×10^{15}	1.6×10^{15}	4.7×10^{14}	4.6×10^{15}	1.6×10^{15}	9.2×10^{14}
Electron density (cm^{-3})	n_e	2.7×10^4	2.8×10^5	8.7×10^6	9.4×10^4	1.6×10^6	6.0×10^6
Initial electron spectral index	p_1	2.7	2.9	3.0	2.6	2.9	3.0
Initial min. electron Lorentz factor	$\gamma_{e,\text{min}}$	2.0×10^2	8.5×10^1	3.5×10^1	7.6×10^1	2.5×10^1	2.2×10^1
Initial max. electron Lorentz factor	$\gamma_{e,\text{max}}$	2.4×10^3	9.2×10^2	9.1×10^2	2.6×10^3	7.4×10^2	3.5×10^2
Injected electron luminosity (erg s^{-1})	L_{inj} ^b	1.3×10^{48}	4.9×10^{47}	1.1×10^{47}	1.6×10^{48}	9.4×10^{47}	9.6×10^{47}
Best fit χ^2	χ^2	79	68	70	73	62	69

^a Effective radius of the elongated jet computed with $R'_E = (3R'_b{}^2 t_{\text{evol}} c/4)^{1/3}$.

^b Jet power in the black hole rest frame.

(SSC) data match. This latter situation only applies at very high $\delta > 60$. If we assume that J0131 is a low-synchrotron-peaked (LSP) source and has $\nu_{\text{sy},pk} < 10^{14}$ Hz, $\delta \leq 30$ may be inferred.

3.4. Modeling the high- N_{H} SED

Because of rapid cooling, the SSC emission is narrow and the high- N_{H} SED (Fig. 3), which is flat across the 0.2–30 keV band, is hard to match with SSC only. However, no X-ray break at a low energy is needed (Fig. 3 bottom) and the minimum e^{\pm} Lorentz factor $\gamma_{e,\text{min}}$ can be small. This moves the EC component to lower frequencies compared to low- N_{H} models (§ 3.3), and the high *NuSTAR* points above 10 keV can be accommodated by the rising part of the EC component (Fig. 4 bottom). Therefore, for modest δ 's both the *WISE*/W3 point and the *NuSTAR* data are well matched, and the minimum $\chi^2 = 62$ (for $\delta=28$) is substantially lower than that of the best low- N_{H} SED fit (Table 2). Clearly a deeper *NuSTAR* exposure with a detection above 30 keV would be a good test of these models. The general parameter trends are similar to the low- N_{H} case; n_e increases while the other parameters decrease with increasing δ .

Comparing across δ in the high- N_{H} case gives results similar to low- N_{H} ; low- δ models conflict with the *WISE*/W3 point, and high- δ values under-predict the *NuSTAR* flux, although the hard X-ray *NuSTAR* points are better matched with the high- N_{H} SED, as noted above. As for the high- N_{H} SED models, our strongest conclusion is a lower limit of $\delta > 6$. Large δ values produce only modest χ^2 increase (e.g., at $\delta = 50$ the increase is only $\Delta\chi^2 \leq 9$ for 6 dofs; 68%), so these large values, while sub-optimal, are still acceptable.

Note that the parameters presented in Table 2 are not unusual for blazar jets, but the inferred B 's are large compared to \leq a few Gauss often used in leptonic models for blazars. It is hard to estimate B in blazar jets model-independently (i.e., from fundamental physics), but >10 G has been invoked in leptonic models (e.g., [Dermer et al. 2014](#)) and even higher ~ 100 G values are used in lepto-hadronic models (e.g., [Bottacini et al. 2016](#)).

3.5. EC models for the SED

We assumed above (§ 3.3) that the X-ray emission is produced by the SSC process, as is usually inferred for blazars. However, in principle disk-EC might dominate, so we check this possibility.

Here suppressing SSC emission with low B , n_e and/or large R_b also suppresses the synchrotron flux. An example (very low $\delta = 2.2$) of such models is presented in Figure 5 along with the low- N_{H} SED. It is easy to match the X-ray SED shape by the EC emission, but the synchrotron emission is very weak and so the *WISE*/W3 point is brighter than the pure disk flux in these models. Increasing δ will make the synchrotron emission even weaker compared to the EC (X-ray) and does not improve the fit. These fits are inferior (e.g., $\chi^2_{\text{min}} \approx 78$ regardless of δ) to the SSC-dominated models in § 3.3 and 3.4 unless the W3 point is attributed to another emission component (e.g., a dust torus). A similar conclusion can be drawn for the high- N_{H} SED. We therefore do not consider these models further.

We note, however, that EC-dominated one-zone models of [Ghisellini et al. \(2015\)](#) with an additional blackbody component for the W3 point appear to explain the SEDs. If it can be shown that the W3 data are produced by blackbody emission, more detailed EC mod-

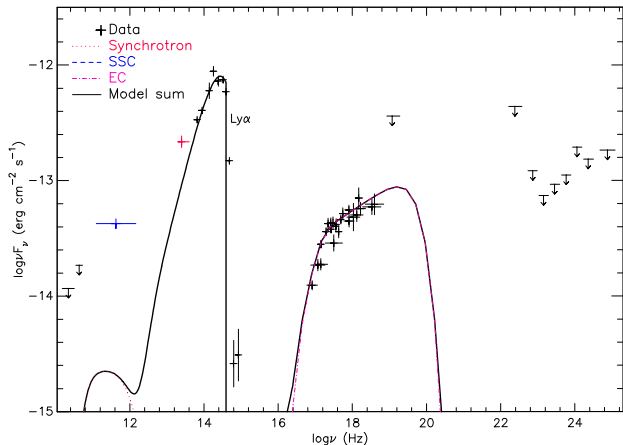


Figure 5. The broadband SED for the low- N_{H} case of J0131 (data points) and an EC model ($\delta = 2.2$) in which X-ray emission is assumed to be produced by the EC process. The SSC emission is too low to be shown in this plot.

eling needs to be carried out; additional 10^{13} – 10^{14} Hz IR data would be very helpful.

4. DISCUSSION AND CONCLUSION

We investigated the X-ray emission of the high- z blazar J0131 using new *NuSTAR* and *XMM* observations, improving on previous studies which relied on limited *Swift* data. We found that the X-ray spectrum can be described by a simple $\Gamma = 1.9$ PL with an absorbing column $N_{\text{H}} = 1.1 \times 10^{21} \text{ cm}^{-2}$ or by a less-absorbed ($N_{\text{H}} = 3.6 \times 10^{20} \text{ cm}^{-2}$) BPL with $\Gamma_1 = 0.5$, $\Gamma_h = 1.8$, and $E_b = 0.7 \text{ keV}$. Intriguingly the hard X-ray ($>10 \text{ keV}$) data seem to suggest that the spectrum is not falling in that band, unlike the high- z blazars B2 1023+25 and QSO J0906+6930 (AR18), although with current data the rise is not highly significant.

We constructed broadband SEDs of the source for both the low- N_{H} and high- N_{H} X-ray cases by supplementing the new X-ray measurements with archival data, and model the SEDs using a synchro-Compton scenario. Because J0131 is not detected by the *Fermi* LAT and there is no sensitive observation in the lower-energy gamma-ray band, our *NuSTAR* measurements provide important constraints on the Compton peak. The X-ray flux could be modeled via two different scenarios: SSC or disk EC. While the EC models can describe the X-ray emission, the models have very low synchrotron flux and do not explain the *WISE*/*W3* point. We considered this less likely and so have focused on the SSC case.

We used a MC technique to explore values of the bulk Doppler factor in these SSC models, finding $\delta > 7$ and $\delta > 6$ (90%) for the low- and high- N_{H} SEDs, respectively. These lower bounds for the J0131 jet seem reasonable

given that radio observations of other high- z blazars infer modest bulk Doppler factors for their radio jets (e.g., $\delta_{\text{radio}} = 13$ and 6 for B2 1023+25 and QSO J0906+6930; Frey et al. 2015; An et al. 2020). However, our lower bound is quite sensitive to the single *WISE*/*W3* data point and would change if the IR flux were lower or higher during the X-ray observation. Interestingly, the disk emission model also under-predicts the *WISE*/*W2* data point at $\approx 7 \times 10^{13} \text{ Hz}$ (Fig. 4). This is also seen in a Kerr black hole disk emission model for J0131 (Fig. 8 of Campitiello et al. 2018). If there is a synchrotron contribution at this frequency, this would tend to increase our δ lower bound. However, since the spectral shape of disk emission around super-massive black holes is poorly known we do not attempt to match the W2 data point with our SED model. Longer wavelength observations will provide more reliable constraints on the synchrotron SED peak.

Some uncertainties are also due to modeling assumptions. For example, if the emission region lies farther away from the black hole than our assumed 0.03 pc, the disk EC emission is suppressed and even higher δ models might be allowed. However, other external emission (dusty torus and broad line region BLR) may contribute to the EC emission. This is only poorly bounded by the LAT upper limits. The distance to the emission region is also related to the large B which we inferred from the models (Table 2). These models demand large B to suppress the EC emission, but a smaller B would be allowed if the region were located farther away. Also, the black hole mass determining the disk temperature and luminosity is also uncertain, although mass and disk SED we used are similar to those inferred in a J0131 Kerr hole disk model ($1.23 \times 10^{10} M_{\odot}$; Campitiello et al. 2018). In general with smaller hole mass, the temperature and luminosity of the disk grow, making the EC component stronger; this is a weak $T \propto M^{-1/4}$ effect. Nevertheless, our $\delta > 6$ lower bound should not be altered since EC emission contributes little to the low- δ models. Note that the parameters in Table 2 are not very extreme. But given that B and δ for other high- z ($z=3$ – 4) blazars are inferred to be modest ($B=1$ – 2 G and $\delta=10$ – 16 ; Paliya et al. 2020), the low- δ (e.g., <20) models may be preferred for J0131.

Using the δ constraints and the formula given in AR18, we infer that there should be >100 (low N_{H}) and >70 (high N_{H}) sources similar to J0131 (see AR18 for details). We cannot yet obtain a firm upper bound on δ directly from the modeling, but assuming that J0131 is an LSP we could set a weak bound $\delta \leq 30$. Then, the inferred number of similar (i.e., J0131-like) blazars would be 230–420 (low N_{H}) or 170–360 (high N_{H}). This may

not be a large improvement compared to the previous results (AR18). However, in the previous work a formal SED fit was not attempted for J0131 due to the lack of X-ray data points, and the model was matched to the SED only by eye. Hence, the new constraints on δ based on formal fits, made possible by the high-quality X-ray data, provide a more accurate population estimate.

Of course, our parameter constraints and population numbers can be tightened by a more complete SED. Sub-mm/IR measurements can pin down the synchrotron flux. The X-ray is the key to the SSC component. A better understanding of the absorption might be obtained with more sensitive soft X-ray or even optical absorption studies. This indirectly affects the inferred X-ray power law, which compared to the synchrotron peak gives us our δ bounds; high sub-mm flux implies larger δ . Since the EC peaks of high- z blazars are expected to lie below the LAT band, the best measurement of the EC component can be made by extending our hard X-ray/soft gamma-ray measurements; a > 10 keV break to a harder spectrum implies an EC peak at low frequency (and a

small δ). Hence, future ALMA, *JWST*, *NuSTAR*, and *AMEGO* (McEnery 2019) observations are warranted to help pin down J0131's beaming and let this member of the very small $z > 5$ jet-dominated QSO sample constrain the high- z blazar population.

ACKNOWLEDGMENTS

We thank the anonymous referee for the careful reading of the paper and insightful comments. This research was supported by Basic Science Research Program through the National Research Foundation of Korea (NRF) funded by the Ministry of Science, ICT & Future Planning (NRF-2017R1C1B2004566).

Facilities: XMM, NuSTAR

Software: HEASoft (v6.26.1; HEASARC 2014), XMM-SAS (v20180620; Gabriel 2017), XSPEC (Arnaud 1996)

REFERENCES

- An, H., & Romani, R. W. 2018, ApJ, 856, 105
- An, T., Mohan, P., Zhang, Y., et al. 2020, Nature Communications, 11, 143
- Arnaud, K. A. 1996, in Astronomical Society of the Pacific Conference Series, Vol. 101, Astronomical Data Analysis Software and Systems V, ed. G. H. Jacoby & J. Barnes, 17
- Berti, E., & Volonteri, M. 2008, ApJ, 684, 822
- Blandford, R. D., & Znajek, R. L. 1977, MNRAS, 179, 433
- Boettcher, M., Mause, H., & Schlickeiser, R. 1997, A&A, 324, 395
- Bottacini, E., Böttcher, M., Pian, E., & Collmar, W. 2016, ApJ, 832, 17
- Burrows, D. N., Hill, J. E., Nousek, J. A., et al. 2005, SSRv, 120, 165
- Campitiello, S., Ghisellini, G., Sbarrato, T., & Calderone, G. 2018, A&A, 612, A59
- Dermer, C. D., Cerruti, M., Lott, B., Boisson, C., & Zech, A. 2014, ApJ, 782, 82
- Fan, X., Narayanan, V. K., Lupton, R. H., et al. 2001, AJ, 122, 2833
- Fermi-LAT Collaboration, Abdollahi, S., Ackermann, M., et al. 2018, Science, 362, 1031
- Frey, S., Paragi, Z., Fogasy, J. O., & Gurvits, L. I. 2015, MNRAS, 446, 2921
- Gabriel, C. 2017, in The X-ray Universe 2017, 84
- Ghisellini, G., Tagliaferri, G., Sbarrato, T., & Gehrels, N. 2015, MNRAS, 450, L34
- Green, G. M., Schlafly, E., Zucker, C., Speagle, J. S., & Finkbeiner, D. 2019, ApJ, 887, 93
- Harrison, F. A., Craig, W. W., Christensen, F. E., et al. 2013, ApJ, 770, 103
- Jansen, F., Lumb, D., Altieri, B., et al. 2001, A&A, 365, L1
- Liodakis, I., Romani, R. W., Filippenko, A. V., et al. 2018, MNRAS, 480, 5517
- Loredo, T. J. 1992, in Statistical Challenges in Modern Astronomy, ed. E. D. Feigelson & G. J. Babu, 275–297
- McEnery, J. 2019, in American Astronomical Society Meeting Abstracts, Vol. 233, American Astronomical Society Meeting Abstracts #233, 158.22
- Paliya, V. S., Ajello, M., Cao, H. M., et al. 2020, arXiv e-prints, arXiv:2006.01857
- Romani, R. W. 2006, AJ, 132, 1959
- Romani, R. W., Sowards-Emmerd, D., Greenhill, L., & Michelson, P. 2004, ApJL, 610, L9
- Sbarrato, T., Tagliaferri, G., Ghisellini, G., et al. 2013, ApJ, 777, 147
- Shakura, N. I., & Sunyaev, R. A. 1973, A&A, 24, 337
- Urry, C. M., & Padovani, P. 1995, PASP, 107, 803

Verner, D. A., Ferland, G. J., Korista, K. T., & Yakovlev,
D. G. 1996, ApJ, 465, 487
Wilms, J., Allen, A., & McCray, R. 2000, ApJ, 542, 914
Yi, W.-M., Wang, F., Wu, X.-B., et al. 2014, ApJL, 795,
L29

Zhang, Y., An, T., Frey, S., et al. 2017, MNRAS, 468, 69